SUPPLEMENTARY INFORMATION
DOI: 10.1038/NNANO.2016.112

Quantum interference in an interfacial superconductor

Srijit Goswami,* Emre Mulazimoglu,* Ana M. R. V. L. Monteiro, Roman Wölbing, Dieter Koelle, Reinhold Kleiner, Ya. M. Blanter, Lieven M. K. Vandersypen, and Andrea D. Caviglia

This supplementary information contains the following:

DOI: 10.1038/NNANO.2016.112

DEVICE FABRICATION

Fig. S1a shows the complete flow of the fabrication processes. Single crystal TiO_2-terminated (001) $SrTiO_3$ (STO) substrates are purchased from CrysTec GmbH© and used without any modification. As discussed in the main text, we fabricate two varieties of SQUIDs: C-SQUID (red arrow) and E-SQUID (brown arrow). Fabrication of the E-SQUID starts with electron beam lithography (EBL) and subsequent deposition of tungsten (W) markers and lift-off. This step is not necessary for the C-SQUID since it requires only a single EBL step. After W deposition (only for the E-SQUID), samples are processed with EBL followed by deposition of amorphous $LaAlO_3$ (a-LAO) via pulsed laser deposition (PLD) to define insulating regions. Subsequent lift-off and optical inspection shows these masked regions (Fig. S1b). Then, crystalline $LaAlO_3$ (c-LAO) is grown via PLD monitored in-situ by reflection high energy electron diffraction (RHEED) to confirm layer-by-layer growth (Fig. S1c). The RHEED diffraction pattern also confirms the two-dimensional nature of the growth (inset of Fig. S1c). Growth of c-LAO is the last fabrication step for C-SQUID. For the E-SQUID, we perform another EBL to define the top gates, followed by metal (Au) evaporation and lift-off. Optical images of a final E-SQUID device are shown in Fig. S1d,e. Ultrasonic wedge bonding is used to make electrical contact to the conducting regions. Further details about each step of the fabrication have been reported previously [1]. We point out two important differences relevant for the devices reported in this study: (i) the c-LAO was grown at a higher temperature of 840°C resulting in a larger critical temperature of the superconductor and (ii) the metallization for the top gates was preceded by a short oxygen plasma exposure to remove polymer residues.

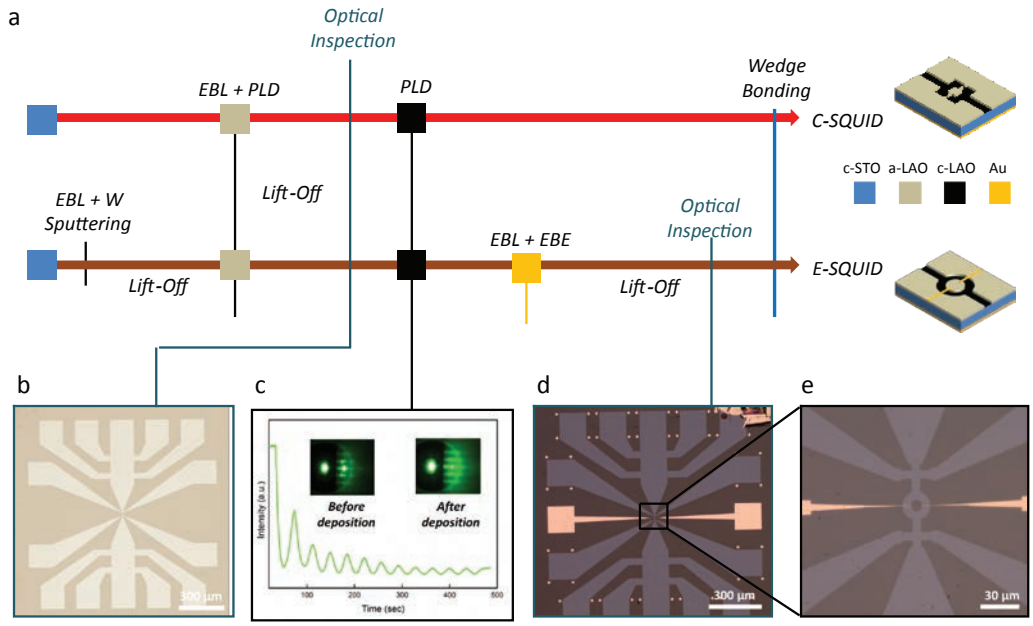

FIG. S1: (a) Fabrication flow for SQUID devices. (b) Optical image after deposition of the amorphous LAO mask. (c) RHEED oscillations obtained during the growth of c-LAO. Inset shows diffraction patterns before/after the growth. (d) Optical image after top gates deposition. (e) Zoom in of (d) showing the active area of a E-SQUID device.

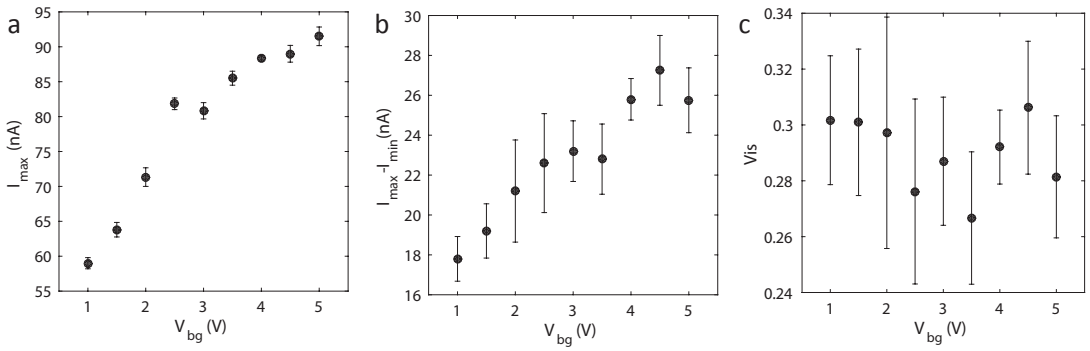

FIG. S2: Error estimates for (a) the maximum critical current I_{max}, (b) $I_{max} - I_{min}$, and (c) visibility for different values of back gate voltage.

ERROR ESTIMATES FOR KINETIC INDUCTANCE

To estimate the error bars for L_k (see Fig. 2d of main text) we analyze the $I_c(\Phi)$ oscillations for each value of V_{bg}. We extract average values of I_{max} and $I_{max} - I_{min}$ (Fig. S2a,b) from 5-6 consecutive oscillations. The error bars represent the mean absolute deviation and Fig. S2c shows the resulting error in *Vis*. We see that *Vis* does not change with V_{bg} and we obtain $Vis \sim 0.29 \pm 0.03$. Since *Vis* is a strong function of β_L and $L_k = \beta_L \Phi_0 / I_{max}$, this uncertainty in *Vis* results in relatively large errors ($\sim 15\%$) on L_k.

TUNING THE E-SQUID

To tune the E-SQUID into the optimal configuration we start by first recording V-Is as each top gate is depleted (with the other grounded). Fig. S3a(b) show such plots for $V_{rg} = 0$ V ($V_{lg} = 0$ V), where the dark/bright regions indicate the superconducting (S)/resistive (R) branch of the V-I curve and the border is representative of the critical current. These plots give us an indication of the action of the individual gates, and allow us to identify values of gate voltage for which the regions below the top gates are being actively depleted (I_c decreases significantly). Next, we keep one gate fixed at a large negative voltage (Fig. S3c) and vary the other. Below a certain gate voltage (indicated by the dashed line) SQUID oscillations begin to appear. To check for the presence of these oscillations we found it particularly convenient to look for $V(\Phi)$ oscillations (as shown in Fig. 1f of the main text), since such measurements are much quicker than $I_c(\Phi)$ measurements.

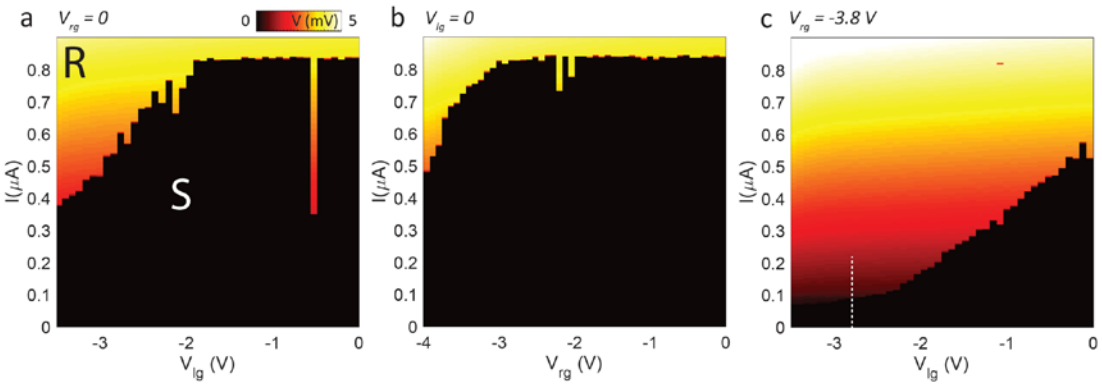

FIG. S3: 2D color maps showing the variation of critical current with (a) V_{lg} varied, $V_{rg} = 0$ V, (b) V_{rg} varied, $V_{lg} = 0$ V, and (c) V_{lg} varied, $V_{rg} = -3.8$ V.

DOI: 10.1038/NNANO.2016.112

FINITE ELEMENT SIMULATIONS

For the simulations of effective area A_{eff} and kinetic inductance L_{k} we use the software package 3D-MLSI [2]. A brief summary of the theoretical background is presented in this section. For more details we refer to [2, 3] and references therein.

Initially, a given superconducting circuitry with thickness t extended in the x-y-plane is subdivided into finite sized triangles (finite element method); cf. Fig. S4a). For each individual element, static London equations are applied to compute the current distribution and the associated magnetic fields for the overall structure under appropriate global boundary conditions. Here, the central figure of merit is the thickness-integrated current density

$$\vec{J}(x,y) = \int \vec{j}(x,y,z)dz = (J_x, J_y) \tag{1}$$

labeled sheet current. As long as t is much smaller than all other dimensions of the superconducting film, the assumption $\nabla \cdot \vec{J}(x,y) = 0$ remains valid and the sheet current can be expressed by a scalar potential g

$$\vec{J}(x,y) = -\hat{z} \times \nabla g = (\frac{\partial g}{\partial y}, -\frac{\partial g}{\partial x}) \tag{2}$$

also called stream function. $g(x,y)$ is calculated for each finite element with $g(x_1,y_1) - g(x_2,y_2)$ being the current crossing any line connecting (x_1,y_1) and (x_2,y_2). Furthermore, $g(x,y)$ can be used to calculate the full energy functional E of the thin film which in turn is closely related to the inductance matrix L comprising self and mutual inductances. By this means, also fluxoids Φ can be calculated for superconducting films containing holes or slits.

For the calculation of effective areas A_{eff} a homogeneous external magnetic field $H = 1\,\mathrm{mA}/\mu\mathrm{m}$ is applied perpendicular to the plane of the SQUID. Boundary conditions are chosen to be $g(x,y) = 0$ at the edge of the SQUID hole as well as at the outer edge of the superconducting structure, i.e. the net current circulating around the hole is $I = 0$. There are diamagnetic currents in each half of the SQUID washer above and below the junctions flowing in counterclockwise direction. The phase gradients produced by these currents can subtract (screening currents) or add (focusing currents) to the ones produced by H such that the fluxoid is the same for any integration path around the SQUID hole. A_{eff} is obtained by computing the fluxoid in the SQUID loop and by $A_{\mathrm{eff}} = \Phi/(\mu_0 H)$, with the

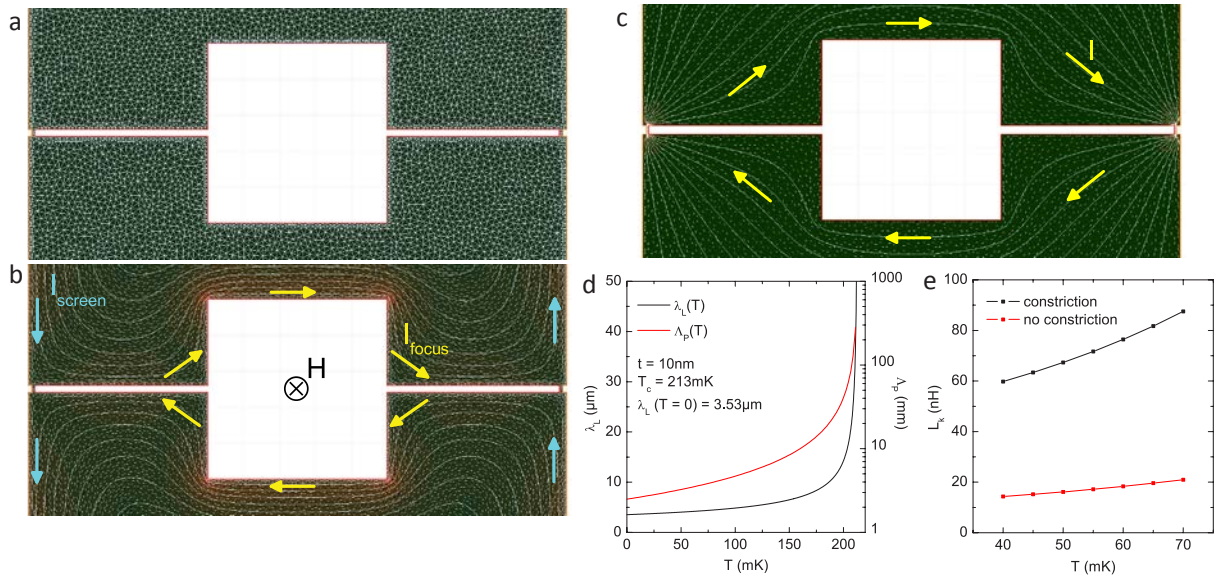

FIG. S4: (a) Example of a mesh used for finite element simulations. Results of numerical simulations for (b) effective area, and (c) kinetic inductance. See text for more details. (d) Calculated temperature dependence of London penetration depth and Pearl length. (e) Calculated temperature dependence of kinetic inductance, with and without constrictions.

vacuum permeability μ_0. Fig. S4b displays the current distribution and $g(x,y)$ for the calculation of $A_{\rm eff}$ for device C-SQ1. Here, white solid lines represent the contour lines of $g(x,y)$. Short white lines indicate $\vec{J}(x,y)$. For a better understanding, $I_{\rm focus}$ and $I_{\rm screen}$ have been emphasized by yellow and cyan arrows, respectively. The color code gives the amplitude of local currents with red and black areas indicating high and low current amplitude, respectively. The numerically estimated values for $A_{\rm eff}$ for C-SQ1, C-SQ2 and E-SQ1 (110.4, 68.6, and 94.8 μm^2 respectively) are in good agreement with the experimentally observed values (111.4, 66.2, 99.6 μm^2), as reflected in Fig. 1g of the main text. We divide the experimentally determined $A_{\rm eff}$ by the area of the central insulating region to obtain flux focussing factors of 4.5, 10.6, 3.3 for C-SQ1, C-SQ2 and E-SQ1 respectively.

Turning to the calculation of the kinetic inductance L_k, the boundary conditions are $g(x,y) = 1\,$mA at the edge of the SQUID hole and $g(x,y) = 0$ at the outer edge of the superconductor, i.e. L_k is computed for a current with amplitude $I = 1\,$mA circulating around the hole (see Fig. S4c). Again, the circulating current I has been emphasized by yellow arrows. Film thickness t and London penetration depth $\lambda_{\rm L}$ are crucial input parameters for the calculation of L_k, however these quantities are initially unknown. We assume $t = 10\,$nm and subsequently adjust $\lambda_{\rm L}$ to reproduce the measured L from the experiments. Choosing $\lambda_{\rm L} = 3.9\,\mu m$, $T = 40\,$mK and $T_{\rm c} = 213\,$mK, we find good agreement between simulation and measurement. We note here, that these values give a Pearl length of $\Lambda_{\rm P} = 2\lambda_{\rm L}^2/t = 3.04\,$mm at $T = 40\,$mK which is of the same order of magnitude as reported elsewhere [4].

As mentioned in the main text, Brandt and Clem [5] have theoretically studied the effects of a large penetration depth on thin film superconducting rings. In the limit $\Lambda_P \to \infty$ they obtain $A_{\rm eff} = \frac{r_a^2 - r_i^2}{2\ln(r_a/r_i)}$, where r_a (r_i) is the outer (inner) radius of the ring. Applying this expression to E-SQ3 ($r_a = 8.1$ μm and $r_i = 3.1$ μm) yields $A_{\rm eff} = 91.6$ μm^2, which is only slightly smaller than the numerically estimated (experimentally determined) values of 94.8 μm^2 (98.6 μm^2). Equation 49 in [5] also allows us to estimate the strength of the Meissner effect in E-SQ3. Using $\Lambda_P = 3$ mm (as inferred above) we find a value of 9×10^{-5} compared to a perfectly shielded ring with the same geometry, showing that the Meissner effect in this structures is indeed very weak.

To reproduce the functional evolution of $L_k(T)$ as seen in the experiments, we implement a temperature dependence of $\lambda_{\rm L}$. We find reasonable agreement for

$$\lambda_{\rm L}(T) = \frac{\lambda_{\rm L}(T=0)}{\sqrt{1 - T/T_{\rm c}}}\ , \tag{3}$$

which is plotted together with the related $\Lambda_{\rm P}(T)$ in Fig. S4d. Note that the same parameters ($\lambda_{\rm L}(T)$, t, $T_{\rm c}$) were used to calculate the effective area at $T = 40\,$mK.

To stress the fact that for device C-SQ1 the dominant contribution to L_k arises from the constriction type Josephson junctions, we compare the behavior of $L_k(T)$ of C-SQ1 with an otherwise equivalent device without constrictions in Fig. S4e. We find that the overall inductance is indeed governed by the contribution of the constrictions by at least a factor of 4. This can be attributed to a large kinetic inductance since the dimensions of the constrictions are well below $\lambda_{\rm L}$.

COMPARISON WITH THE RCSJ MODEL

In our experiments we found that the nature of the V-I curves (value of critical current, shape of the transition to the resistive branch) depends on the back gate voltage. Since our estimates of L_k rely on the conversion of visibility (Vis) to β_L, we implicitly assume that the resistively and capacitively shunted junction (RCSJ) model [6, 7] appropriately describes our system. Below, we briefly describe the RSCJ model and how it relates to our C-SQUID devices.

To model an asymmetric SQUID we consider the circuit shown in Fig. S5a. The Josephson junctions are described by Josephson currents with phases δ_1 and δ_2 and amplitudes $I_{01} = I_0(1 - a_i)$ and $I_{02} = I_0(1 + a_i)$, resistors $R_1 = R/(1 - a_r)$ and $R_2 = R/(1 + a_r)$, and capacitors $C_1 = C(1 - a_c)$ and $C_1 = C(1 + a_c)$. The Nyquist noise arising from the two resistors is described by two independent current noise sources I_{N1} and I_{N2} having white spectral power densities $4k_BT/R_1$ and $4k_BT/R_2$, respectively and k_B is the Boltzmann constant. The two arms of the SQUID loop have inductances $L_1 = L(1 - a_l)/2$ and $L_1 = L(1 + a_l)/2$. The total inductance L is the sum of the geometric (L_g) and the kinetic (L_k) inductance. The loop is biased with a current I. A flux Φ_{ext} is applied to the loop. In the following we normalize currents to I_0, fluxes to the flux quantum Φ_0, voltages to I_0R and time to $\Phi_0/2\pi I_0R$. We further use the McCumber parameter $\beta_c = 2\pi I_0R^2C/\Phi_0$, the inductance parameter $\beta_L = 2I_0L/\Phi_0$ and the noise parameter $\Gamma = 2\pi k_BT/(I_0\Phi_0)$. With these units the SQUID is described by the differential equations [8, 9]

DOI: 10.1038/NNANO.2016.112

$$i/2 + j = \beta_c(1 - a_c)\ddot{\delta_1} + (1 - a_r)\dot{\delta_1} + (1 - a_i)\sin\delta_1 + i_{N1} \tag{4}$$

$$i/2 - j = \beta_c(1 + a_c)\ddot{\delta_2} + (1 + a_r)\dot{\delta_2} + (1 + a_i)\sin\delta_2 + i_{N2}\ . \tag{5}$$

Here i and j denote the normalized bias current and circulating current in the SQUID loop and the dots denote derivatives with respect to normalized time. The spectral densities of the normalized noise currents i_{N1} and i_{N2} are given by $4\Gamma(1 - a_r)$ and $4\Gamma(1 + a_r)$, respectively. The circulating current j is given by

$$j = \frac{1}{\beta_L}\left(\frac{\delta_2 - \delta_1}{\pi} - 2\Phi_{ext} + a_l\beta_L\frac{i}{2}\right)\ . \tag{6}$$

From these equations we get the time dependent (high frequency) voltages across the junctions via the second Josephson relation, $\dot{\delta_k} = u_k$, (k = 1,2). The dc (i.e. low frequency) voltage v across the SQUID is obtained by averaging $(u_1 + u_2)/2$ over sufficiently long times. From the dc voltage v one obtains current voltage (IV) characteristics i vs. v, the SQUID voltage modulation v vs. Φ_{ext}, the transfer function $dv/d\Phi_{ext}$ or the modulation of the critical current i_c vs. Φ_{ext} and $Vis = (i_{max} - i_{min})/i_{max}$. For the simulations discussed here we assumed symmetric parameters, i.e. $a_i = a_r = a_c = a_l = 0$. Calculations for $\Gamma = 0$ are shown in Fig. 2c of main text.

For higher values of back gate voltage V_{bg}, I_c is significantly larger showing a distinct switch in the V-I curves. Here we find a reasonable agreement with the RCSJ model. For example for $V_{bg} = 4$ V (Fig. 2b of main text) numerical simulations give $\beta_L \sim 2.3$ and $\beta_c \sim 5.5$ for the noiseless case. Including thermal fluctuations ($\Gamma = 0.015$), we find an upper limit for $\beta_c \sim 15$. In either case, since $\beta_c > 1$, we expect to observe hysteretic V-I curves. The experimental V-I trace (Fig. S5b.) clearly displays such a hysteresis. Furthermore, we observe a distinct bump-like feature in the return branch of the curve (red trace). In the RCSJ framework, this structure arises due to an LC resonance from the circuit shown in Fig. S5a. One would then expect that $eV_0 = \hbar\omega = 1/\sqrt{LC/2}$. Here $V_0 \approx 120\ \mu$V is the position of the feature and ω is the resonance frequency. Using the experimentally determined value of $L_k \approx 50$ nH we estimate $C \approx 1$ fF. Finally using $I_0 = 44$ nA and $R = 8$ kΩ we obtain $\beta_c \approx 10$. This is indeed consistent with values of β_c predicted by the RCSJ model. Therefore, this analysis shows that (a) the RCSJ model describes our system reasonably well and (b) our estimates of L_k from the I_c oscillations are indeed reliable.

We found that the V-I curves at lower back gate voltage (as in Fig. 1e of the main text) could not be reproduced well within the RCSJ framework. In particular, we see a large excess current, which could be indicative of non-equilibrium processes or even a multi-valued current-phase relation. Furthermore, the low value of the critical current makes the effects of thermal noise much more significant, thus making it difficult to reliably extract the kinetic inductance. We therefore restrict our analysis to $V_{bg} \geq 1$ V (as seen in Fig. 2d of the main text).

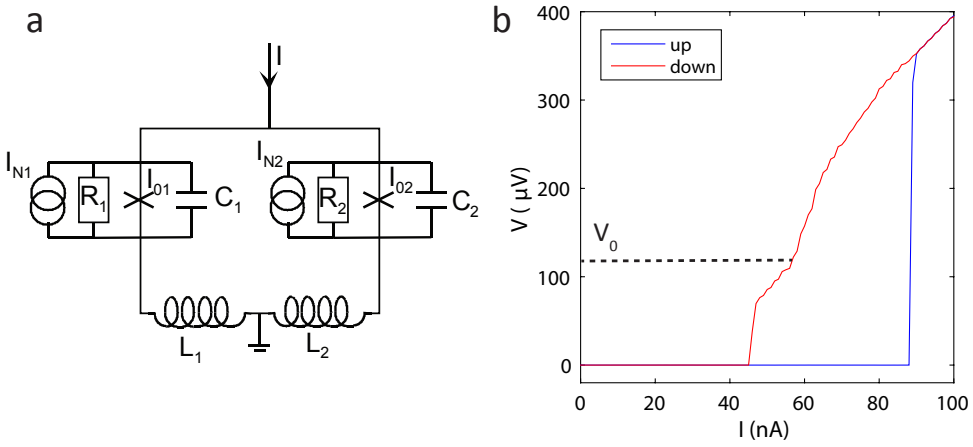

FIG. S5: (a) Circuit for RCSJ model. (b) Experimental V-I trace at $V_{bg} = 4$ V, showing hysteresis. V_0 indicates the position of an LC resonance.

* Equal contributions

[1] S. Goswami, E. Mulazimoglu, L. M. K. Vandersypen, and A. D. Caviglia, Nano Letters **15**, 2627 (2015).
[2] M. M. Khapaev, M. Y. Kupriyanov, E. Goldobin, and M. Siegel, Superconductor Science and Technology **16**, 24 (2003).
[3] E. H. Brandt, Phys. Rev. B **72**, 024529 (2005).
[4] J. A. Bert, K. C. Nowack, B. Kalisky, H. Noad, J. R. Kirtley, C. Bell, H. K. Sato, M. Hosoda, Y. Hikita, H. Y. Hwang, et al., Phys. Rev. B **86**, 060503 (2012).
[5] E. H. Brandt and J. R. Clem, Phys. Rev. B **69**, 184509 (2004).
[6] W. C. Stewart, Applied Physics Letters **12** (1968).
[7] D. E. McCumber, Journal of Applied Physics **39** (1968).
[8] C. D. Tesche and J. Clarke, Journal of Low Temperature Physics **29**, 301 (1977).
[9] J. Bruines, V. de Waal, and J. Mooij, Journal of Low Temperature Physics **46**, 383 (1982).